Research Square

Preprints are preliminary reports that have not undergone peer review.
They should not be considered conclusive, used to inform clinical practice,
or referenced by the media as validated information.

A Flexible Nanoporous Iridium Oxide Epidural Interface for Repeated Cervical Neuromodulation after Ischemic Stroke

Xu Guozheng

xu-gz@163.com

1. The First School of Clinical Medicine, Southern Medical University; 2. Department of Neurosurgery, General Hospital of Central Theater Command

Zhao Pengcheng

1. The First School of Clinical Medicine, Southern Medical University; 2. Department of Neurosurgery, General Hospital of Central Theater Command

Dongxu Ma

Peking University

Li Keyuan

1.Medical College, Wuhan University of Science and Technology;2.Department of Neurosurgery, General Hospital of Central Theater Command

Li Huanhuan

1. The First School of Clinical Medicine, Southern Medical University; 2. Department of Neurosurgery, General Hospital of Central Theater Command

Zhou Henan

Department of Neurosurgery, General Hospital of Central Theater Command

Zhang Yongning

Department of Neurosurgery, General Hospital of Central Theater Command

Liu Zhezhi

1.Medical College, Wuhan University of Science and Technology;2.Department of Neurosurgery, General Hospital of Central Theater Command

Zhihong Li

Peking University

Song Jian

1. The First School of Clinical Medicine, Southern Medical University; 2. Department of Neurosurgery, General Hospital of Central Theater Command

---

Article

Keywords: cervical spinal cord stimulation, flexible neural interface, ischemic stroke, motor recovery, synaptic plasticity

Posted Date: November 13th, 2026

DOI: https://doi.org/10.21203/rs.3.rs-11470052/v1

License: This work is licensed under a Creative Commons Attribution 4.0 International License. Read Full License

Additional Declarations: There is no conflict of interest

Abstract

Flexible cervical epidural interfaces must accommodate spinal motion while maintaining efficient charge transfer and reliable performance during repeated stimulation. We developed a four-contact polyimide epidural interface incorporating nanoporous sputtered iridium oxide (IrOx) for repeated cervical spinal cord stimulation (SCS) after experimental ischemic stroke. Compared with gold, the IrOx surface exhibited approximately sevenfold greater nanoscale roughness, reduced the impedance at 1 kHz from approximately 8.2 to 0.7 kΩ, and increased cathodic charge-storage and charge-injection capacities from 0.061 to 3.6 mC cm^{-2} and from 0.041 to 1.11 mC cm^{-2}, respectively. The interface maintained electrical continuity during 10,000 bending cycles and retained measurable electrochemical function after four weeks of implantation, without a statistically detectable increase in local cervical Iba1 or GFAP signals relative to non-implanted MCAO controls. In rats subjected to middle cerebral artery occlusion/reperfusion, 14 daily SCS sessions initiated on post-stroke day 4 improved neurological function, forelimb strength, and gait coordination. Several functional differences remained detectable on day 32, 14 days after stimulation cessation. T2-defined lesion volume was lower on day 18 but not day 32, indicating that later functional differences were not explained solely by lesion modification. Cortical transcriptomic, histological, structural, and electrophysiological analyses associated SCS with reduced inflammatory responses and partial recovery of neuronal and synaptic measures. This flexible nanoporous IrOx interface therefore integrates micro/nanoscale electrode engineering with medium-term in vivo reliability and enables longitudinal investigation of cervical neuromodulation after stroke.

1. Introduction

Implantable neural interfaces for repeated neuromodulation must combine mechanical compliance, stable tissue contact, and efficient electrochemical charge transfer. Flexible polymer microdevices can reduce bending stiffness and conform more closely to soft or curved neural tissues, while microfabricated electrode arrays enable spatially confined stimulation and recording[1,2]. However, reducing electrode dimensions also decreases the geometric surface area available for charge transfer, which generally increases impedance and constrains reversible charge delivery. Increasing the electrochemically active surface area through micro- and nanoscale surface engineering is therefore an important strategy for improving electrode performance without enlarging the physical device footprint[3]. These requirements are particularly demanding for cervical epidural interfaces, where restricted anatomical space and spinal motion challenge tissue conformity, contact stability, and mechanical durability.

Stroke remains a leading cause of long-term neurological disability, with persistent motor impairment contributing substantially to chronic dependence[4,5]. Cervical spinal cord stimulation (SCS) has emerged as a potential approach for augmenting residual motor function after stroke[6]. Epidural stimulation near the cervical dorsal-root entry zones recruits large-diameter sensory afferents and modulates the excitability of spinal interneuronal and motor circuits receiving residual descending input[7,8]. Clinical

studies have demonstrated improvements in upper-limb strength and movement control in individuals with chronic post-stroke hemiparesis during repeated cervical SCS[9,10]. Nevertheless, the extent to which functional benefits remain detectable after stimulation has ended remains incompletely defined, and the biological changes accompanying repeated stimulation are not well understood[11]. Experimental stroke models provide opportunities to investigate these questions, but their use requires cervical interfaces capable of reproducible implantation and repeated stimulation over longitudinal experimental periods.

An appropriate small-animal cervical interface must be sufficiently thin and compliant to accommodate spinal motion while providing low-impedance contacts, adequate charge-injection capacity, mechanical durability, and limited local tissue reactivity. Recent studies have employed polyimide as a microfabrication-compatible flexible substrate for lightweight integrated neural probes and scalable high-density cortical microelectrode arrays[12,13]. At the electrode–tissue interface, iridium oxide (IrOx) can support reversible Faradaic charge transfer and provide a substantially larger electrochemically active surface area than planar noble-metal contacts[3,14]. Nanostructured and sputtered IrOx microelectrodes have consequently demonstrated low impedance and high charge-storage and charge-injection capacities, although their performance depends strongly on surface morphology, deposition conditions, and stimulation parameters[15]. However, the integration of nanoporous IrOx contacts into a flexible cervical epidural platform has not been sufficiently evaluated under repeated post-stroke stimulation, mechanical loading, medium-term implantation, and longitudinal functional assessment within the same experimental system.

Here, we developed a flexible polyimide epidural interface incorporating four nanoporous sputtered IrOx contacts for repeated cervical SCS in rats. We characterized its surface morphology, electrochemical performance, mechanical durability, four-week in vivo functionality, and local cervical tissue response. In a rat model of middle cerebral artery occlusion/reperfusion, stimulation was initiated on post-stroke day 4 and delivered daily for 14 days. Longitudinal behavioral testing and T2-weighted magnetic resonance imaging were combined with cortical transcriptomics, histology, immunofluorescence, dendritic-spine analysis, and whole-cell electrophysiology. This integrated design enabled the micro/nanoengineered interface, repeated cervical stimulation, persistent functional outcomes, and associated cortical responses to be evaluated within a single experimental framework.

2. Results

2.1 Design, fabrication, and in vitro performance of the flexible nanoporous IrOx epidural interface

The flexible cervical epidural interface was designed as a 58-mm-long polyimide device comprising a four-contact stimulation region, a ribbon interconnect region, and a rear connector region (Fig. 1a). Each circular stimulation contact had a diameter of 0.5 mm, with a center-to-center spacing of 2 mm. This

compact contact configuration was designed for epidural positioning across the C5–T1 spinal segments while maintaining mechanical conformity to the cervical spinal cord.

The device was fabricated from a double-sided copper-clad polyimide film using a combination of flexible-circuit and microfabrication processes (Fig. 1b). Briefly, the circuit patterns were defined by dry-film photolithography and copper etching, followed by laser micromachining of the conductive vias and device outline. An insulating cover layer with patterned contact openings was subsequently laminated onto the device. The electrode-contact stack, consisting of 5 nm titanium, 100 nm gold, 5 nm iridium, and approximately 200 nm IrOx, was deposited through an aligned stainless-steel shadow mask. Finally, a female connector was soldered to the rear interface pads to form the completed four-contact epidural device.

The surface morphology of the electrode contacts was examined to determine the structural changes produced by IrOx deposition (Fig. 1c–f). Scanning electron microscopy showed that the sputtered Au surface had a relatively smooth and compact granular morphology (Fig. 1c), whereas the IrOx-coated surface exhibited a dense nanoporous nanostructure with substantially greater topographical complexity (Fig. 1e). Consistent with these observations, atomic force microscopy revealed a root-mean-square roughness (Rq) of 1.59 nm for Au and 11.2 nm for IrOx (Fig. 1d,f), corresponding to an approximately sevenfold increase in nanoscale surface roughness following IrOx deposition.

Electrochemical impedance spectroscopy showed that the IrOx-modified electrodes had a lower impedance magnitude than the Au electrodes across the measured frequency range (Fig. 1g). At 1 kHz, the impedance decreased from approximately 8.2 kΩ for Au to 0.7 kΩ for IrOx, representing a reduction of more than tenfold (Fig. 1h). The IrOx-modified electrodes also exhibited a smaller phase lag at 1 kHz. Cyclic voltammetry showed a markedly larger enclosed current–voltage area for IrOx than for Au (Fig. 1i). The corresponding cathodic charge-storage capacity was 3.6 mC cm^{-2} for IrOx and 0.061 mC cm^{-2} for Au, representing an approximately 59-fold difference.

Voltage transients were subsequently recorded under symmetric biphasic current pulses of increasing amplitude to estimate the charge-injection limits of the two electrode interfaces (Fig. 1j–m). For the IrOx-modified electrode, cathodic polarization increased progressively with stimulation current (Fig. 1j). Linear extrapolation to the predefined cathodic polarization limit yielded an estimated maximum current (Imax) of 2.17 mA and a charge-injection capacity of 1.11 mC cm^{-2} (Fig. 1k). Under the same experimental conditions, the Au electrode showed an estimated Imax of 0.08 mA and a charge-injection capacity of 0.041 mC cm^{-2} (Fig. 1l,m). Thus, the nanoporous IrOx interface supported a substantially higher estimated charge-injection limit than the unmodified Au interface under the tested in vitro conditions.

Mechanical and electrical durability was evaluated by cyclic bending and ultrasonication. During 10,000 bending cycles at a bending radius of 2 mm, the device resistance remained within approximately 4.3–4.6 Ω (Fig. 1n). After 100 min of ultrasonication, the relative changes in impedance magnitude and phase were − 3.97% and − 22.9%, respectively (Fig. 1o). No loss of electrical continuity or increase in

impedance was detected under the applied bending and ultrasonication conditions, supporting the functional durability of the flexible interface before in vivo implantation.

a) Layout and dimensions of the flexible four-contact cervical epidural interface. b) Schematic illustration of the device-fabrication process. c,d) Representative scanning electron microscopy (SEM) and atomic force microscopy (AFM) images of the gold (Au) electrode surface. e,f) Representative SEM and AFM images of the nanoporous IrOx-coated electrode surface. g) Electrochemical impedance magnitude and phase spectra of the Au and IrOx-modified electrodes. h) Impedance magnitude and phase at 1 kHz. i) Cyclic voltammetry curves of the Au and IrOx-modified electrodes. j,l) Representative voltage transients of the IrOx-modified (j) and Au (l) electrodes under symmetric biphasic current pulses of increasing amplitude. k,m) Relationships between applied current and maximum cathodic polarization used to estimate the maximum current (Imax) and charge-injection capacity of the IrOx-modified (k) and Au (m) electrodes. n) Resistance of the IrOx-modified flexible devices during 10,000 bending cycles at a bending radius of 2 mm. o) Relative changes in impedance magnitude and phase during 100 min of ultrasonication. Quantitative data are presented as mean ± SD from 12 independently fabricated devices (n = 12).

2.2 Four-week in vivo functional retention and local cervical tissue response

To evaluate the functional retention of the flexible IrOx interface during longitudinal implantation, devices were retrieved after four weeks in vivo and examined macroscopically and electrochemically. The explanted devices retained their overall geometry, with no visible fracture of the flexible carrier or conductive traces, and all four electrode contacts remained identifiable (Fig. 2a). At 1 kHz, the mean impedance increased from approximately 727 Ω before implantation to 1387 Ω after four weeks in vivo, corresponding to an increase of approximately 91%, whereas the phase response showed only a modest descriptive change (Fig. 2b; n = 6 devices). Despite the increase in impedance, electrical continuity and measurable electrochemical function were retained after the four-week implantation period.

The local cervical tissue response to the combined implantation and stimulation procedure was assessed by immunofluorescence staining for ionized calcium-binding adaptor molecule 1 (Iba1) and glial fibrillary acidic protein (GFAP). Cervical spinal cord sections spanning the C4–T1 segments were collected from the electrode-implanted SCS group and anatomically matched non-implanted MCAO/R controls. Representative images showed Iba1-positive microglia and GFAP-positive astrocytes in both groups (Fig. 2c). In the implanted group, the region of interest was defined as spinal cord tissue located within 1–2 mm of the electrode implantation site; anatomically corresponding regions were analyzed in the non-implanted control group. Quantitative analysis detected no statistically significant between-group differences in either Iba1 or GFAP fluorescence intensity at the four-week endpoint (both $P > 0.05$). Thus, under the tested conditions, the combined implantation and stimulation procedure was not associated with a statistically detectable increase in either glial marker relative to the non-implanted MCAO/R control. Because an implanted but unstimulated group was not included in this comparison, the

individual contributions of implantation and electrical stimulation to the local tissue response could not be distinguished.

a) Representative photographs of devices retrieved after four weeks in vivo, showing preservation of the overall device geometry, conductive traces, and electrode-contact sites. b) Electrode impedance magnitude and phase at 1 kHz before implantation and after four weeks in vivo (n = 6 devices). Measurements before and after implantation were obtained from the same devices. c) Representative immunofluorescence images of DAPI, Iba1, GFAP, and merged channels in cervical spinal cord sections from the electrode-implanted SCS group and non-implanted MCAO/R controls, together with the corresponding quantification of Iba1 and GFAP fluorescence intensities. Data are presented as mean ± SEM. ns, not significant. Scale bars, 50 μm.

2.3 System-Level Validation of Repeated Cervical SCS after MCAO/R

Behavioral testing was performed according to the timeline shown in Fig. 3a. Neurological deficits, forelimb grip strength, and gait were assessed at the indicated time points. On day 2, before electrode implantation and stimulation, modified Neurological Severity Score (mNSS) values did not differ between the MCAO + sh-SCS and MCAO + SCS groups ($P > 0.05$). Both MCAO groups had higher mNSS scores than the Sham group (both adjusted $P < 0.001$). The two MCAO groups remained comparable on day 11 ($P > 0.05$). From day 18 onward, mNSS scores were lower in the MCAO + SCS group than in the MCAO + sh-SCS group on days 18, 25, and 32 (all adjusted $P < 0.05$). Sham animals maintained near-zero scores and differed from both MCAO groups at each time point (all adjusted $P < 0.001$; Fig. 3d).

Forelimb grip strength was evaluated on days 18 and 32 (Fig. 3b,e). Grip strength normalized to body weight was lower in the MCAO + sh-SCS group than in the Sham group at both time points (both adjusted $P < 0.05$). The normalized grip strength was higher in the MCAO + SCS group than in the MCAO + sh-SCS group on days 18 and 32 (both adjusted $P < 0.05$). This between-group difference remained detectable at the post-stimulation assessment on day 32.

Gait was evaluated on days 2, 18, and 32 using automated spatiotemporal analysis (Fig. 3c). On day 2, none of the measured gait parameters differed between the MCAO + sh-SCS and MCAO + SCS groups (all adjusted $P > 0.05$). Compared with Sham animals, both MCAO groups exhibited lower regularity indices, gait symmetry indices, and bilateral stance-phase durations, together with longer swing-phase durations (all adjusted $P < 0.001$). These results showed comparable baseline gait impairment between the two MCAO groups.

On day 18, the MCAO + SCS group exhibited higher regularity and gait symmetry indices than the MCAO + sh-SCS group (both adjusted $P < 0.05$). Right forelimb stance-phase duration was also higher, whereas right forelimb and hindlimb swing-phase durations were lower in the MCAO + SCS group (all adjusted $P < 0.05$). Right hindlimb stance-phase duration did not differ between the two groups (adjusted $P > 0.05$). On day 32, the MCAO + SCS group retained a higher regularity index (adjusted $P < 0.01$), gait symmetry

index, and right forelimb stance-phase duration (both adjusted $P < 0.05$). Right hindlimb stance-phase duration and bilateral swing-phase durations did not differ between the two MCAO groups at this time point (all adjusted $P > 0.05$; Fig. 3f–k).

2.4 Longitudinal Evolution of T2-Defined Lesion Volume

T2-weighted MRI was performed on days 2, 18, and 32 after MCAO to evaluate longitudinal changes in lesion burden (Fig. 4a). No T2-hyperintense lesion was detected in the Sham group. On day 2, before electrode implantation and stimulation, lesions in both MCAO groups were predominantly located in the ipsilateral cortex and striatum (Fig. 4b). Neither absolute nor normalized T2-defined lesion volume differed between the MCAO + sh-SCS and MCAO + SCS groups at this time point (both adjusted $P > 0.05$). Thus, the two groups had comparable baseline lesion burdens before treatment.

On day 18, after 14 daily stimulation sessions, absolute T2-defined lesion volume was lower in the MCAO + SCS group than in the MCAO + sh-SCS group (80.30 ± 2.42 versus 94.41 ± 2.60 mm^3; adjusted P = 0.0068). Normalized lesion volume was also lower in the MCAO + SCS group (38.66 ± 1.41% versus 44.60 ± 1.57%; adjusted P = 0.0447; Fig. 4b). On day 32, neither absolute nor normalized lesion volume differed between the two MCAO groups (both adjusted P > 0.11). Thus, cervical SCS was associated with smaller T2-defined lesion measures on day 18, whereas no between-group difference was detected on day 32.

2.5 Cervical SCS is associated with partial reversal of post-stroke cortical transcriptional changes

Principal component analysis revealed group-dependent shifts in cortical transcriptomic profiles, with Sham samples clustering separately from the two MCAO groups and greater dispersion among MCAO + sh-SCS samples (Fig. 5a). Using a stringent threshold of FDR < 0.05 and |log2 fold change| > 1, 2,392 differentially expressed genes (DEGs; 1,943 upregulated and 449 downregulated) were identified in MCAO + sh-SCS animals relative to Sham animals (Fig. 5b). In contrast, cervical SCS altered a smaller set of 39 DEGs relative to MCAO + sh-SCS animals, including 8 upregulated and 31 downregulated genes (Fig. 5c). Of these, 29 genes showed significant bidirectional reversal across both comparisons: 24 genes induced by MCAO were suppressed by SCS, whereas 5 genes reduced by MCAO were increased by SCS (Fig. 5d).

Gene set enrichment analysis provided broader evidence of coordinated transcriptional reprogramming despite the limited number of individual DEGs after SCS. SCS positively enriched synaptic processes, including postsynaptic specialization assembly, synaptic vesicle priming, calcium ion-regulated neurotransmitter exocytosis, glutamate receptor activity, and postsynaptic density assembly (NES = 2.16–2.41, FDR < 0.05). Conversely, pathways related to tumor necrosis factor and interleukin-6 production, complement activation, neutrophil migration, and macrophage activation were negatively enriched (NES = − 1.96 to − 2.08, FDR < 0.05; Fig. 5e). Directional comparison further showed that MCAO-

associated activation of complement and coagulation, NF-κB signaling, Toll-like receptor signaling, phagosome, cytokine–receptor interaction, complement activation, and neutrophil migration was reversed by SCS. Conversely, the MCAO-associated suppression of calcium ion-regulated neurotransmitter exocytosis was reversed toward positive enrichment after SCS (Fig. 5f). Together, these findings indicate that cervical SCS partially redirects the post-stroke cortical transcriptional state from inflammatory activation toward synaptic organization and neurotransmission.

2.6 Histopathological, Myelin, and Glial Changes after Cervical SCS

H&E staining revealed marked cortical disorganization and vacuolar degeneration in the MCAO + sh-SCS group, whereas these histopathological alterations were attenuated in the MCAO + SCS group (Fig. 6b). LFB staining further showed greater preservation of myelin in the MCAO + SCS group (Fig. 6c). Two-way ANOVA identified significant effects of group, time, and their interaction on relative LFB integrated optical density (all $P \leq 0.0082$). Compared with MCAO + sh-SCS, MCAO + SCS significantly increased relative LFB integrated optical density on both Day 18 and Day 32 (adjusted $P = 0.0293$ and 0.0444, respectively; Fig. 6d).

Immunofluorescence staining demonstrated pronounced microglial and astrocytic activation after MCAO/R (Fig. 6e). Significant group, time, and group-by-time interaction effects were detected for both Iba-1 and GFAP expression (all $P \leq 0.0085$). Compared with MCAO + sh-SCS, MCAO + SCS significantly reduced Iba-1 expression on Day 18 and Day 32 (adjusted $P = 0.0018$ and 0.0300, respectively; Fig. 6f), with corresponding reductions in GFAP expression (adjusted $P = 0.0014$ and 0.0161, respectively; Fig. 6g). Collectively, these results indicate that cervical SCS alleviates post-ischemic histopathological damage, preserves myelin integrity, and suppresses sustained glial reactivity.

2.7 Neuronal, Neurotrophic, and Synaptic-Associated Protein Expression after Cervical SCS

Immunofluorescence staining showed that NeuN, BDNF, PSD95, and MAP-2 expression in the ipsilateral M1 cortex was reduced in the MCAO + sh-SCS group compared with the Sham group on both Day 18 and Day 32 (all adjusted $P \leq 0.01$; Fig. 7). Compared with MCAO + sh-SCS, MCAO + SCS significantly increased NeuN expression on Day 18 and Day 32 (adjusted $P = 0.0019$ and 0.0193, respectively; Fig. 7a,b) and produced corresponding increases in BDNF expression (adjusted $P = 0.0052$ and 0.0402; Fig. 7a,c). MCAO + SCS also increased PSD95 expression (adjusted $P = 0.0182$ and 0.0237; Fig. 7d,e) and MAP-2 expression (adjusted $P = 0.0215$ and 0.0118; Fig. 7d,f) at the two respective time points.

Two-way ANOVA identified significant group and time effects for all four markers (all $P \leq 0.05$). Significant group-by-time interactions were detected for NeuN, PSD95, and MAP-2 ($P = 0.0161$, 0.0112, and < 0.0001, respectively), but not for BDNF ($P = 0.1732$). Collectively, these results indicate that cervical

SCS partially preserves neuronal integrity and promotes the recovery of neurotrophic and synaptic-associated protein expression after MCAO/R.

a, Representative immunofluorescence images of DAPI (blue), NeuN (red), BDNF (green), and merged staining in the ipsilateral M1 cortex of the Sham, MCAO + sh-SCS, and MCAO + SCS groups on Day 18 and Day 32. **b, c**, Quantification of the relative fluorescence intensities of NeuN (b) and BDNF (c). **d**, Representative immunofluorescence images of DAPI (blue), PSD95 (red), MAP-2 (green), and merged staining in the ipsilateral M1 cortex on Day 18 and Day 32. **e, f**, Quantification of the relative fluorescence intensities of PSD95 (e) and MAP-2 (f). Data are presented as mean ± SEM; $n = 5$ animals per group at each time point. Statistical significance was assessed using two-way ANOVA followed by Tukey's multiple-comparisons test. The brackets indicate comparisons between the MCAO + sh-SCS and MCAO + SCS groups. *$P < 0.05$ and **$P < 0.01$. Scale bars are shown in the images.

2.8 Dendritic-Spine and Excitatory Synaptic Measures after Cervical SCS

Golgi–Cox staining revealed substantial dendritic spine loss in ipsilateral M1 pyramidal neurons following MCAO/R (Fig. 8a). One-way ANOVA showed significant group differences in both spine density and total spine number (both $P < 0.0001$). Compared with MCAO + sh-SCS, MCAO + SCS significantly increased dendritic spine density (adjusted $P = 0.0113$; Fig. 8b) and total spine number (adjusted $P = 0.0047$; Fig. 8c). However, both measurements remained lower than those in the Sham group (adjusted $P = 0.0012$ and 0.0001, respectively), indicating partial structural recovery.

Whole-cell patch-clamp recordings further showed significant group differences in miniature excitatory postsynaptic current (mEPSC) frequency and amplitude (both ANOVA $P = 0.0002$; Fig. 8d). Compared with MCAO + sh-SCS, MCAO + SCS significantly increased mEPSC frequency (adjusted $P = 0.0338$; Fig. 8e) and amplitude (adjusted $P = 0.0200$; Fig. 8f), although both remained below Sham levels (adjusted $P = 0.0221$ and 0.0255, respectively). These results indicate that cervical SCS partially restores dendritic spine integrity and excitatory synaptic transmission after MCAO/R.

3. Discussion

This study developed a flexible four-contact cervical epidural interface incorporating a nanoporous IrOx stimulation layer and evaluated its performance in a rat model of ischemic stroke. The principal contribution is the integration of device-level engineering validation with longitudinal neuromodulation and multimodal biological assessment. The IrOx interface provided lower impedance and greater charge-storage and estimated charge-injection capacities than Au, while the polyimide platform maintained electrical continuity during mechanical testing and four weeks of implantation. Using this interface, repeated cervical SCS was associated with improvements in neurological function, forelimb strength, and gait coordination. Several functional differences remained detectable on day 32, 14 days after stimulation had ceased. These outcomes were accompanied by temporally dependent changes in T2-defined lesion volume and cortical molecular, histological, structural, and electrophysiological

measures. The biological findings nevertheless remain associative and do not establish a single causal mechanism linking cervical stimulation to cortical remodeling.

The electrochemical performance of the interface was primarily attributable to the nanoporous IrOx contact layer. Compared with Au, IrOx increased nanoscale surface roughness by approximately sevenfold, reduced impedance at 1 kHz by more than tenfold, and increased cathodic charge-storage capacity by approximately 59-fold. The estimated charge-injection capacity also increased from 0.041 to 1.11 mC cm^{-2} under the tested in vitro conditions. These findings are consistent with the increased electrochemically active surface area and reversible Faradaic charge transfer reported for iridium oxide neural interfaces[16,17]. The device also maintained a resistance of approximately 4.3–4.6 Ω during 10,000 bending cycles at a radius of 2 mm. However, these accelerated bench-top tests do not fully reproduce the combined mechanical, electrochemical, and biological stresses encountered during cervical implantation.

After four weeks in vivo, the electrode impedance at 1 kHz increased from approximately 727 to 1387 Ω, corresponding to an increase of approximately 91%. The device should therefore be described as retaining functional electrical performance rather than maintaining unchanged electrochemical stability. The increase may reflect several processes, including adsorption of biological material, peri-electrode tissue formation, changes in the electrode–electrolyte interface, or modification of the IrOx layer. The present experiments did not include post-explantation surface microscopy, elemental analysis, or quantitative coating-adhesion measurements and therefore cannot distinguish among these possibilities. Nevertheless, the devices retained electrical continuity and supported the complete 14-session stimulation protocol, establishing their feasibility for longitudinal experiments over the tested four-week period.

At the four-week endpoint, Iba1 and GFAP fluorescence in the cervical spinal cord did not differ significantly between the implanted and stimulated animals and the anatomically matched non-implanted MCAO/R controls. This finding indicates that the combined implantation and stimulation procedure was not associated with a statistically detectable increase in these two glial markers under the tested conditions. It does not, however, independently establish implant biocompatibility or stimulation safety. An implanted but unstimulated group was not included in this comparison, and Iba1 and GFAP intensities alone cannot resolve cell-specific activation states or more subtle tissue responses. Future device-validation studies should include non-implanted surgical controls, implanted unstimulated animals, and implanted stimulated animals, together with quantitative histopathology and post-explantation material analysis.

Clinical studies have shown that cervical epidural SCS can acutely improve strength, upper-limb kinematics, and motor control in people with chronic post-stroke hemiparesis[9,10]. Recent evidence indicates that cervical SCS can also enhance postsynaptic reciprocal inhibition and reduce pathological muscle co-activation[18]. These observations support the view that stimulation of cervical dorsal-root afferents modulates spinal interneuronal and motor-pool excitability, thereby increasing the

responsiveness of spinal circuits to residual descending commands[18–20]. In the present study, active SCS improved multiple behavioral measures relative to implanted sham-stimulation controls. Importantly, several differences remained detectable on day 32, 14 days after the final stimulation session. Although these findings do not demonstrate permanently retained recovery, they suggest that the observed effects were not limited to immediate stimulation-dependent facilitation. Repeated stimulation may have provided a permissive spinal state in which successful sensorimotor activity was reinforced over successive sessions. Direct recordings from dorsal-root, propriospinal, corticospinal, or reticulospinal pathways will be required to determine which circuits mediated these effects.

The longitudinal MRI results further indicate that changes in lesion burden alone do not fully explain the behavioral findings. T2-defined lesion volume was lower in the MCAO + SCS group on day 18, whereas no between-group difference was detected on day 32. T2-weighted signal during the subacute and chronic phases reflects a combination of water content, cavitation, gliosis, and tissue remodeling and should not be interpreted as a stage-independent measurement of irreversible neuronal loss[21,22]. The day-18 difference may therefore reflect altered edema resolution, secondary injury, inflammation, or tissue remodeling. Because several behavioral differences persisted on day 32 in the absence of a detectable lesion-volume difference, preservation of T2-defined tissue alone appears insufficient to account for the later functional outcomes. Reorganization of surviving sensorimotor networks provides a plausible complementary explanation[23].

The cortical measurements were consistent with a partial, rather than complete, shift toward a recovery-associated state. Only a relatively modest number of differentially expressed genes distinguished MCAO + SCS from MCAO + sh-SCS animals, and the transcriptional findings should therefore not be described as global cortical “reprogramming.” Nevertheless, gene-set enrichment indicated attenuation of selected inflammatory programs and enrichment of pathways related to synaptic organization, vesicle priming, and neurotransmitter release. These changes coincided with lower cortical Iba1 and GFAP signals, higher NeuN, BDNF, PSD95, and MAP2 signals, greater dendritic-spine density, and partial recovery of miniature excitatory postsynaptic current frequency and amplitude. Reactive microglia and astrocytes have heterogeneous and time-dependent functions after stroke, including both tissue-supportive and potentially synapse-removing activities[24–26]. Experimental studies have shown that reactive glial cells can engulf synaptic elements after ischemic stroke and that inhibition of selected phagocytic pathways can reduce synapse loss and improve neurological outcomes[27,28]. However, the present study did not measure glial phagocytosis or manipulate an inflammatory pathway. The data therefore support an association among cervical SCS, selected inflammatory responses, and synaptic recovery, but do not demonstrate that suppression of glial activity caused the observed synaptic or behavioral effects.

The structural and electrophysiological findings provide complementary evidence for partial synaptic recovery. Increased PSD95 and MAP2 signals, greater dendritic-spine density, and higher miniature excitatory postsynaptic current frequency and amplitude were directionally consistent with improved excitatory synaptic function. However, changes in miniature current frequency and amplitude can arise

from multiple presynaptic and postsynaptic processes and cannot uniquely identify the underlying adaptation[29]. Moreover, several measurements remained different from Sham levels, arguing against complete normalization of the injured cortex[30,31]. Increased use of the affected limb represents an important alternative or complementary explanation. Rehabilitative motor activity can stabilize newly formed dendritic spines and reorganize peri-infarct cortical networks[32,33]. By facilitating limb use, SCS may have increased the amount or quality of self-generated motor practice[20]. This activity-dependent mechanism would remain therapeutically relevant but cannot be distinguished from direct spinal-to-cortical or inflammation-related effects in the present study.

Several limitations define the scope of these conclusions. The study used young adult male rats, whereas sex, age, and vascular comorbidities influence stroke recovery. The four-week implantation period was insufficient to establish long-term coating stability, implant safety, or functional durability. The local tissue-response experiment lacked an implanted but unstimulated control, and Iba1 and GFAP did not provide cell-state or implant-specific information. Some outcome-specific cohorts were small, limiting statistical precision and the assessment of inter-animal heterogeneity. Stimulation parameters were selected from pilot experiments without a systematic multidimensional dose–response analysis. Direct recordings of recruited spinal and descending pathways were not performed. Bulk RNA sequencing lacked cellular resolution, and the molecular measurements were not designed to establish causal relationships. Finally, although MRI was longitudinal, several histological, molecular, and electrophysiological outcomes were obtained from terminal cohorts; individual trajectories linking lesion evolution, inflammation, synaptic remodeling, and functional recovery could therefore not be determined.

In conclusion, the flexible nanoporous IrOx epidural interface combined low-impedance stimulation contacts, enhanced charge-transfer performance, mechanical flexibility, and four-week in vivo functional retention in a small-animal cervical platform. The interface enabled repeated cervical SCS after experimental ischemic stroke and linked longitudinal stimulation with sustained motor differences and cortical changes consistent with compensatory plasticity. The dissociation between day-32 behavioral outcomes and T2-defined lesion volume suggests that later functional differences cannot be attributed solely to lesion preservation. Longer-term device validation, implant-only controls, direct circuit recordings, activity-matched rehabilitation groups, cell-resolved analyses, and pathway-specific perturbations will be required to establish the durability, mechanism, and translational potential of this approach.

4. Methods

4.1 Electrode design and fabrication

The layout and fabrication workflow of the flexible cervical epidural interface are shown in Fig. 1a,b. The electrode has an overall length of 58 mm and consists of three main regions: the front electrode contact region, the middle ribbon interconnect region, and the rear electrode interface region. The electrode

contains four stimulation contacts, each with a diameter of 0.5 mm and an inter-contact spacing of 2 mm.

The electrode was fabricated using standard flexible printed circuit and microfabrication processes. The detailed fabrication procedure is as follows: (I) A double-sided copper-clad polyimide (PI) film was used as the starting substrate. (II) Dry-film photoresist was patterned to define the circuit traces. (III) The copper layer was then etched to form the conductive traces. One side contains the electrode interconnect lines, while the other side contains only the bonding pads. (IV) Laser micromachining was performed to create via holes at the bonding pad locations and to define the electrode outline. (V) An insulating cover layer with patterned openings was laminated onto the front side. (VI) A stainless-steel shadow mask was aligned and attached to the front side, followed by sputter deposition of titanium, gold, iridium, and iridium oxide onto the electrode contact sites and bonding pad regions. (VII) After sputtering, the shadow mask was removed. (VIII) Finally, a female connector was soldered to the interface pads, yielding the completed electrode device.

4.2 IrOx deposition.

Iridium oxide (IrO_x) was deposited by reactive magnetron sputtering. A 3-inch iridium target (99.95% purity) was used as the sputtering source. Prior to IrO_x deposition, a 5 nm titanium layer, a 100 nm gold layer, and a 5 nm iridium layer was sequentially sputtered under a power of 100 W, a working pressure of 0.2 Pa, and an argon flow rate of 25 sccm. For IrO_x deposition, the sputtering power was set to 200 W, yielding a deposition rate of approximately 40 nm/min. The total IrO_x thickness was about 200 nm. During deposition, the working pressure was maintained at 1.28 Pa, with argon and oxygen flow rates of 200 sccm and 50 sccm, respectively.

4.3 Electrode characterization.

The surface morphology of the electrodes was characterized using SEM (Sigma 300, ZEISS) and AFM (Dimension Icon, Bruker). SEM imaging was carried out using the InLens detector at an accelerating voltage of 10 kV with a working distance of approximately 5 mm to examine the surface microstructure of the electrode interfaces. AFM measurements were performed in tapping mode over a scan area of 2 μm × 2 μm, with an image resolution of 256 × 256 pixels. The electrochemical performance of the electrodes was evaluated in 1× phosphate-buffered saline (PBS) using a three-electrode configuration. The electrode under test served as the working electrode, while a platinum mesh and an Ag/AgCl electrode were used as the counter and reference electrodes, respectively. Electrochemical impedance spectroscopy (EIS) was performed over a frequency range of 100 Hz to 100 kHz with a 50 mV sinusoidal excitation signal. Cyclic voltammetry (CV) was carried out within a potential window of − 0.6 to 0.8 V at a scan rate of 0.2 V s^{-1} to determine the charge storage capacity (CSC). Voltage transients were recorded using biphasic symmetric charge-balanced current pulses with gradually increased current amplitudes. The maximum cathodic voltage excursion was extracted from each transient curve, and the safe current limit (I_{max}) was determined by linear fitting of the voltage excursion versus applied current, with the intersection at the cathodic water reduction limit (− 0.6 V) defined as the maximum safe stimulation

current. CIC was calculated as $CIC=I_{max}\times PW/A$, where Imax is the maximum safe current, PW is the pulse width per phase, and A is the electrode contact geometric area. Fatigue bending tests were carried out using a custom-built cyclic bending apparatus to evaluate the mechanical durability of the electrodes. The samples were subjected to cyclic bending at a rate of 100 cycles per minute, and their electrical and structural stability were monitored during the test. Furthermore, to evaluate the adhesion stability of the IrO_x coating, the electrodes were subjected to ultrasonication in deionized water at 40 kHz, and the impedance and phase were measured every 10 min.

4.4 Animals and Experimental Groups

A total of 72 adult male Sprague Dawley rats (8 weeks old, 260 to 280 g) were purchased from Hunan SJA Laboratory Animal Co., Ltd. (production license no. SCXK(Xiang) 2021-0002). Animals were maintained under specific pathogen-free conditions at 22 ± 1°C with a relative humidity of 50 ± 10% under a 12 h light/dark cycle, with free access to food and water. All animals were acclimatized for 7 days before experimentation. All experimental procedures were approved by the Institutional Animal Care and Use Committee (approval no. JWS-202504-020) and were conducted in accordance with the relevant guidelines for laboratory animal care and use.

Sample size estimation was performed a priori using G*Power 3.1 based on preliminary experimental data. Under conditions of a two-tailed test, α = 0.05, power = 0.80, and Cohen's d = 1.2, the minimum required sample size was calculated to be 10 animals per group. Considering potential mortality and modeling failure, 12 animals were initially allocated to each group. Randomization was performed by an independent statistician using a computer-generated random number table after stratification according to baseline neurological scores. No significant differences in baseline neurological function were observed among groups (all $P > 0.05$). Behavioral testing, histological analyses, and data quantification were performed by investigators blinded to group allocation throughout the study.

An independent cohort design was adopted. Animals were divided into two subcohorts according to tissue collection time points: week 2 (W2, day 18 after MCAO) and week 4 (W4, day 32 after MCAO). Each subcohort consisted of three experimental groups: (1) Sham group, in which animals underwent cervical vessel exposure without filament insertion or electrode implantation and served as surgical controls; (2) MCAO + sh-SCS group, in which animals underwent MCAO surgery and electrode implantation without electrical stimulation to control for surgical manipulation and implantation effects; and (3) MCAO + SCS group, in which animals underwent MCAO surgery and electrode implantation followed by 14 consecutive days of epidural spinal cord stimulation. Electrical stimulation was delivered using a 16-channel constant-current stimulator (Acimicro NanoST, Acimicro Medical Technology Co., Ltd.) with symmetric biphasic charge-balanced pulses. This stimulation paradigm minimizes net charge accumulation and reduces the risk of irreversible electrochemical reactions at the electrode–tissue interface, thereby improving stimulation safety and electrode stability.

4.5 MCAO/R Model Preparation

A left-sided middle cerebral artery occlusion/reperfusion (MCAO/R) model was established using a modified intraluminal filament technique[34]. Rats were anesthetized with sodium pentobarbital (35 mg/kg, intraperitoneal injection) and placed in the supine position. Following a midline cervical incision, the left common carotid artery, internal carotid artery, and external carotid artery were carefully isolated by blunt dissection. A lysine-coated nylon monofilament (diameter 0.36 mm; Beijing Cinontech Co., Ltd.) [35] was introduced through the common carotid artery and advanced gently to occlude the origin of the middle cerebral artery. After 90 min of occlusion, the filament was slowly withdrawn to allow reperfusion. Core body temperature was maintained at 37°C during surgery using a thermostatically controlled heating pad. Sham-operated animals underwent identical surgical procedures except for filament insertion. Postoperative analgesia and local antiseptic treatment were administered routinely.

Neurological deficits were evaluated 48 h after surgery using the modified Neurological Severity Score (mNSS). Only rats with mNSS values between 7 and 12 were included in subsequent experiments, whereas sham-operated animals were expected to exhibit scores ≤ 2.

4.6 Cervical Spinal Electrode Implantation

On day 3 after MCAO, rats were anesthetized with isoflurane (3.0% induction and 1.5% maintenance; oxygen flow rate 1 L/min) and positioned prone. A 2 cm midline incision was made over the C3 to C7 vertebral region. Under microscopic guidance, the paraspinal muscles were separated by blunt dissection. The ligamentum flavum was carefully exposed approximately 2 mm lateral to the midline at the right C4 to C5 intervertebral space using a blunt microsurgical dissector. The flexible electrode was inserted into the epidural space through a minimally invasive puncture approach and positioned over the C5 to T1 spinal cord segments. The electrode body was secured to the surrounding paraspinal fascia. Lead wires were tunneled subcutaneously to the cranial surface, and the connector was fixed to the skull using dental cement. Incisions were closed layer by layer, and topical antibiotic ointment was applied to prevent postoperative infection.

4.7 Spinal Cord Stimulation Protocol

Motor threshold (MT) was determined individually before each stimulation session to achieve personalized stimulation intensity. Measurements were performed in awake rats under mild restraint. Stimulation was initially delivered at 1 Hz with a pulse width of 200 μs. Current intensity was increased gradually in increments of 0.1 mA starting from 0.1 mA until rhythmic low-amplitude contractions of the ipsilateral forelimb or shoulder musculature were visually observed without generalized tonic activity or signs of distress.

Epidural spinal cord stimulation in the MCAO + SCS group began on day 4 after MCAO. Stimulation parameters were set at a frequency of 50 Hz, pulse width of 200 μs, and stimulation intensity corresponding to 90% of the individual MT. Each stimulation session lasted 60 min and was administered once daily for 14 consecutive days. Animals in the MCAO + sh-SCS group underwent identical handling and electrode connection procedures without electrical output. Body weight,

spontaneous locomotor activity, and wound healing were monitored daily during the intervention period. Stimulation programming and parameter allocation were performed by an independent investigator to maintain blinding throughout the study.

4.8 Neurological Function Assessment

Modified Neurological Severity Score

Global neurological function was evaluated longitudinally using the mNSS at day 2 after MCAO and on days 11, 18, 25, and 32 after MCAO. The mNSS includes motor, sensory, reflex, and balance assessments, with total scores ranging from 0 to 18. Higher scores indicate more severe neurological impairment[36].

Forelimb Grip Strength

Forelimb grip strength was measured on days 18 and 32 after MCAO using a digital grip strength meter (XR501, Shanghai Xinruan Information Technology Co., Ltd.). Each animal underwent five consecutive measurements of maximal forelimb contractile force. The highest and lowest values were excluded, and the remaining three measurements were averaged. Results were normalized to body weight and expressed as the grip strength/body weight ratio (g/g) to minimize the influence of inter-animal body weight variation[37].

Gait Analysis

Gait performance was evaluated at baseline (day 2 after MCAO), day 18, and day 32 using the VisuGait automated gait analysis system (Shanghai Xinruan Information Technology Co., Ltd.). Animals traversed freely along a 30 × 100 cm transparent corridor while gait parameters were recorded automatically. Three valid trials were included for analysis for each animal. A valid trial was defined as uninterrupted traversal completed within 2 to 8 s with a walking speed coefficient of variation ≤ 15%. Primary gait parameters included regular step sequence ratio, gait symmetry index, right forelimb and hindlimb stance duration, and right forelimb and hindlimb swing duration[38].

4.9 MRI Imaging

T2-weighted magnetic resonance imaging was performed on days 2, 18, and 32 after MCAO using a 9.4-T small-animal MRI scanner (uMR 9.4T, United Imaging Healthcare, Wuhan, China). Day 2 imaging was performed before electrode implantation and stimulation to confirm successful model establishment and assess baseline lesion severity. Day 18 imaging was conducted after 14 consecutive days of cervical spinal cord stimulation to evaluate subacute lesion evolution, whereas day 32 imaging was performed at the chronic experimental endpoint. During scanning, rats were maintained under isoflurane anesthesia (1.5–2.0%) in the prone position. T2-weighted images were acquired using the following parameters: repetition time/echo time (TR/TE), 3,000/45.64 ms; field of view, 34 × 34 mm^2; slice thickness, 0.3 mm; and 33 contiguous coronal slices without interslice gaps.

Image analysis was performed using ImageJ software by an investigator blinded to group allocation. On each coronal section, the hyperintense ischemic lesion and the contralateral cerebral hemisphere were manually delineated. Absolute infarct volume was calculated as the sum of the lesion area across all sections multiplied by the slice thickness:

$$V_{\text{infarct}} = \sum_{i=1}^{n} A_{\text{infarct},i} \times t$$

where $A_{\text{infarct},i}$ represents the infarct area on section i, and t represents the slice thickness. To account for inter-animal differences in brain size, infarct volume was additionally normalized to the contralateral hemisphere volume and expressed as a percentage:

$$\text{Normalized infarct volume } (\%) = \frac{V_{\text{infarct}}}{V_{\text{contralateral hemisphere}}} \times 100$$

Both the absolute infarct volume and the normalized infarct volume were used for subsequent statistical analyses[39].

4.10 RNA Sequencing and Bioinformatic Analysis

On day 14 of SCS intervention, ipsilateral M1 cortical tissue was collected using a 2 mm tissue punch, immediately frozen in liquid nitrogen, and stored at − 80°C. Total RNA was extracted using TRIzol reagent. Samples meeting quality control criteria (RNA integrity number ≥ 7.0 and OD260/280 ≥ 1.8) were subjected to paired-end sequencing (150 bp, ≥ 20 Gb clean reads per sample) using the Illumina NovaSeq 6000 platform.

Sequencing reads were aligned to the rat reference genome (Rnor_6.0) using STAR software. Differential gene expression analysis was performed using DESeq2 with thresholds of |log2 fold change| > 1 and false discovery rate (FDR) < 0.05. Differentially expressed genes were further analyzed using Gene Ontology enrichment, Kyoto Encyclopedia of Genes and Genomes pathway analysis, and Reactome annotation. Statistical significance was defined as FDR < 0.05.

4.11 Tissue Harvesting and Histopathological Assessment

At the designated endpoint, rats were deeply anesthetized with sodium pentobarbital (60 mg/kg) and transcardially perfused with 0.9% saline followed by 4% paraformaldehyde. Brain tissues and cervical spinal cord segments (C5 to T1) were collected and post-fixed in 4% paraformaldehyde for 4 to 6 h, followed by cryoprotection in sequential 20% and 30% sucrose solutions until tissues sank completely. Samples were embedded in OCT compound and rapidly frozen in liquid nitrogen.

Coronal cryosections were prepared at a thickness of 20 μm using a 1:5 serial sampling strategy, corresponding to one section every 100 μm, covering approximately 2 mm anterior and posterior to the ipsilateral primary motor cortex (M1). Hematoxylin and eosin staining was used to evaluate neuronal morphology and tissue architecture, whereas Luxol Fast Blue staining was used to assess myelin

integrity. Whole-slide images were acquired using a 20× objective scanner. At least five sections per animal were analyzed, and the average value per animal was used for statistical analysis.

4.12 Immunofluorescence Staining

Sections were permeabilized with 0.3% Triton X-100 for 20 min and blocked with 5% normal goat serum for 1 h, followed by overnight incubation at 4°C with primary antibodies. Primary antibodies included anti-Iba1 (1:500, Wako), anti-GFAP (1:500, Abcam), anti-NeuN (1:400, Millipore), anti-BDNF (1:200, Santa Cruz), anti-MAP2 (1:300, Abcam), and anti-PSD95 (1:200, Cell Signaling Technology). Sections were subsequently incubated with fluorescence-conjugated secondary antibodies for 2 h at room temperature, counterstained with DAPI, and imaged using a confocal microscope (Leica SP8 or equivalent).

Fluorescence quantification was performed using ImageJ software. Three regions of interest (200 × 200 μm) were selected from anatomically matched areas within the ipsilateral M1 cortex. Fluorescence intensity was normalized to the dorsal horn signal intensity at the distal T2 to T3 spinal level as an internal reference. At least five sections per animal were analyzed, and three regions per section were averaged. NeuN-positive neurons located within cortical layers V to VI were quantified using the Cell Counter plugin with manual verification, and results were expressed as cells/mm².

4.13 Golgi-Cox Staining

Freshly isolated brain tissues were immersed in Golgi fixation solution (G1069-20ML, Servicebio, Wuhan, China) for 48 h. Samples were then rinsed repeatedly with phosphate-buffered saline and transferred to Golgi impregnation solution for 2 weeks in the dark. Coronal sections (60 μm) were prepared using a cryostat and subsequently developed, dehydrated in graded ethanol, cleared with xylene, and mounted with neutral resin.

Pyramidal neurons within the M1 cortex were imaged using a microscope equipped with a 100× oil-immersion objective and sequential Z-stack acquisition. Dendritic spine analyses were performed using Fiji/ImageJ software. For each animal, at least five non-overlapping secondary apical or basal dendritic segments with lengths ≥ 20 μm were analyzed independently. Total spine density and the proportions of thin, mushroom, and stubby spines were quantified. All imaging and quantitative analyses were performed under blinded conditions.

4.14 Patch Clamp Electrophysiology

On day 14 of SCS treatment, rats were sacrificed and brains were rapidly transferred into ice-cold oxygenated artificial cerebrospinal fluid saturated with 95% O_2 and 5% CO_2. Coronal brain slices (300 μm) were prepared using a vibrating microtome (Leica VT1200S) and allowed to recover in oxygenated artificial cerebrospinal fluid at room temperature for 1 h.

Patch pipettes were fabricated from borosilicate glass capillaries with resistances of 3 to 6 MΩ and filled with intracellular solution containing (in mM): K-gluconate 130, KCl 10, HEPES 10, EGTA 0.5, MgATP 4, Na_2GTP 0.3, and phosphocreatine 10. The pH was adjusted to 7.3 and osmolality to 290 to 295 mOsm.

Miniature excitatory postsynaptic currents were recorded from layer V pyramidal neurons in the ipsilateral M1 cortex using the whole-cell configuration at a holding potential of − 70 mV. Tetrodotoxin (1 μM) was added to block action potential-dependent activity, whereas bicuculline (20 μM) was applied to inhibit GABAA receptor-mediated inhibitory currents. Signals were sampled at 10 kHz and filtered at 4 kHz. Event detection was performed using MiniAnalysis software in semi-automated mode with an amplitude threshold corresponding to approximately three times the root mean square noise level (approximately 5 pA). At least 5 min of stable recordings were analyzed per neuron, and a minimum of five neurons per animal were included for analysis.

4.15 Statistical Analysis

Statistical analyses were performed using GraphPad Prism 10.1 (GraphPad Software, Boston, MA, USA). Data are presented as the mean ± SEM, with the animal considered the experimental unit; multiple sections, regions of interest, dendritic segments, or recorded neurons from the same animal were averaged before analysis. Two-group comparisons were performed using two-tailed paired or unpaired Student's *t*-tests, as appropriate. Single-time-point comparisons among three groups were analyzed by one-way ANOVA, whereas longitudinal behavioral and MRI data obtained from the same animals were analyzed by two-way repeated-measures ANOVA. Histological and immunofluorescence data obtained from different animals at days 18 and 32 were analyzed by ordinary two-way ANOVA with group and endpoint as between-subject factors. ANOVA was followed by Tukey's multiple-comparisons test. RNA-sequencing data were analyzed using DESeq2 with Benjamini–Hochberg correction, and differential expression was defined as $|\log2 \text{ fold change}| > 1$ and FDR < 0.05. All tests were two-sided, and $P < 0.05$ was considered statistically significant.

Declarations

Competing interests

The authors declare no competing interests.

Acknowledgements

This work was supported by the Hubei Provincial Key Research and Development Program (2025BCB123), Hubei Provincial Clinical Medical Research Center for Minimally Invasive Treatment of Cerebrovascular Diseases, Brain Science and Brain-like Intelligence Technology-National Science and Technology Major Project (2025ZD0215200), Science and Technology Innovation Program of Xiongan New Area (2025XAGG0031), and National Natural Science Foundation of China (62374005).

Data availability

The data that support the findings of this study have been included in the main text and Supplementary Information. All other relevant data supporting the findings of this study are available from the corresponding authors upon request.

References

1. Steins, H. *et al.* A flexible protruding microelectrode array for neural interfacing in bioelectronic medicine. *Microsyst Nanoeng* 8, 131 (2022).
2. Guo, Z. *et al.* A flexible neural implant with ultrathin substrate for low-invasive brain–computer interface applications. *Microsyst Nanoeng* 8, 133 (2022).
3. Amini, S. *et al.* Sustainability inspired fabrication of next generation neurostimulation and cardiac rhythm management electrodes via reactive hierarchical surface restructuring. *Microsyst Nanoeng* 10, 125 (2024).
4. GBD 2021 Nervous System Disorders Collaborators. Global, regional, and national burden of disorders affecting the nervous system, 1990–2021: a systematic analysis for the Global Burden of Disease Study 2021. *Lancet Neurol* 23, 344–381 (2024).
5. Feigin, V. L. *et al.* World Stroke Organization: Global Stroke Fact Sheet 2025. *International Journal of Stroke* 20, 132–144 (2025).
6. Allen, J. R., Karri, S. R., Yang, C. & Stoykov, M. E. Spinal Cord Stimulation for Poststroke Hemiparesis: A Scoping Review. *Am J Occup Ther* 78, 7802180220 (2024).
7. McIntosh, J. R. *et al.* Intraoperative electrical stimulation of the human dorsal spinal cord reveals a map of arm and hand muscle responses. *Journal of Neurophysiology* 129, 66–82 (2023).
8. Balaguer, J.-M. *et al.* Neural mechanisms underlying the recovery of voluntary control of motoneurons after paralysis with spinal cord stimulation. *Neuron* 113, 3846–3862.e6 (2025).
9. Powell, M. P. *et al.* Epidural stimulation of the cervical spinal cord for post-stroke upper-limb paresis. *Nat Med* 29, 689–699 (2023).
10. de Freitas, R. M. *et al.* Spinal cord stimulation for upper limb motor function in people with chronic post-stroke hemiparesis: a feasibility trial. *Nat Med* 32, 2579–2590 (2026).
11. Zhang, T. *et al.* Recent advances in potential mechanisms of epidural spinal cord stimulation for movement disorders. *Experimental Neurology* 392, 115330 (2025).
12. Zhou, C. *et al.* Through-polymer, via technology-enabled, flexible, lightweight, and integrated devices for implantable neural probes. *Microsyst Nanoeng* 10, 54 (2024).
13. Hettick, M. *et al.* Minimally invasive implantation of scalable high-density cortical microelectrode arrays for multimodal neural decoding and stimulation. *Nat. Biomed. Eng* 10, 1206–1221 (2025).
14. Maeng, J. *et al.* Stability of sputtered iridium oxide neural microelectrodes under kilohertz frequency pulsed stimulation. *J. Neural Eng.* 21, 066019 (2024).
15. Schelles, M. *et al.* Optimization of sputtered iridium oxide microelectrodes for long-term intracortical stimulation. *Biomed. Phys. Eng. Express* 11, 055034 (2025).

16. Frederick, R. A., Meliane, I. Y., Joshi-Imre, A., Troyk, P. R. & Cogan, S. F. Activated iridium oxide film (AIROF) electrodes for neural tissue stimulation. *J. Neural Eng.* 17, 056001 (2020).
17. Lutz, H. M. *et al.* Analysis of electrochemical impedance spectroscopy data for sputtered iridium oxide electrodes. *J. Neural Eng.* 22, 036007 (2025).
18. Borda, L. *et al.* Spinal cord stimulation modulates post-synaptic inhibition to improve arm neuromotor control after chronic stroke. *Cell Reports Medicine* 7, 102925 (2026).
19. Kathe, C. *et al.* The neurons that restore walking after paralysis. *Nature* 611, 540–547 (2022).
20. Pirondini, E. *et al.* Poststroke arm and hand paresis: should we target the cervical spinal cord? *Trends Neurosci* 45, 568–578 (2022).
21. Sicard, K. M., Henninger, N., Fisher, M., Duong, T. Q. & Ferris, C. F. Long-Term Changes of Functional MRI–Based Brain Function, Behavioral Status, and Histopathology After Transient Focal Cerebral Ischemia in Rats. *Stroke* 37, 2593–2600 (2006).
22. Karki, K. *et al.* Chronic brain tissue remodeling after stroke in rat: A 1-year multiparametric magnetic resonance imaging study. *Brain Research* 1360, 168–176 (2010).
23. Ismail, U. N., Yahya, N. & Manan, H. A. Investigating functional connectivity related to stroke recovery: A systematic review. *Brain Res* 1840, 149023 (2024).
24. Prescott, K. *et al.* Blocking of microglia-astrocyte proinflammatory signaling is beneficial following stroke. *Front Mol Neurosci* 16, 1305949 (2023).
25. Tang, Y. *et al.* Single-Cell RNA Sequencing Reveals Microglial Heterogeneity and Functional States After Cerebral Ischemia-Reperfusion Injury. *JIR* Volume 18, 16931–16956 (2025).
26. Shang, T., Kuang, B., Shang, Y. & Zou, W. Microglia-Astrocyte Crosstalk in Post-Stroke Neuroinflammation: Mechanisms and Therapeutic Strategies. *CN* 23, 1645–1665 (2025).
27. Wu, C. *et al.* STING inhibition suppresses microglia-mediated synapses engulfment and alleviates motor functional deficits after stroke. *J Neuroinflammation* 21, 86 (2024).
28. Karaganova, I. & Mindova, S. Neuroplasticity after stroke: Adaptive and maladaptive mechanisms in evidence-based rehabilitation. *Journal of Stroke and Cerebrovascular Diseases* 35, 108634 (2026).
29. Koesters, A. G., Rich, M. M. & Engisch, K. L. Diverging from the Norm: Reevaluating What Miniature Excitatory Postsynaptic Currents Tell Us about Homeostatic Synaptic Plasticity. *Neuroscientist* 30, 49–70 (2024).
30. Brown, C. E., Li, P., Boyd, J. D., Delaney, K. R. & Murphy, T. H. Extensive Turnover of Dendritic Spines and Vascular Remodeling in Cortical Tissues Recovering from Stroke. *J. Neurosci.* 27, 4101–4109 (2007).
31. Murphy, T. H. & Corbett, D. Plasticity during stroke recovery: from synapse to behaviour. *Nat Rev Neurosci* 10, 861–872 (2009).
32. Clark, T. A. *et al.* Rehabilitative Training Interacts with Ischemia-Instigated Spine Dynamics to Promote a Lasting Population of New Synapses in Peri-Infarct Motor Cortex. *J. Neurosci.* 39, 8471–8483 (2019).

33. Kim, S. Y., Hsu, J. E., Husbands, L. C., Kleim, J. A. & Jones, T. A. Coordinated Plasticity of Synapses and Astrocytes Underlies Practice-Driven Functional Vicariation in Peri-Infarct Motor Cortex. *J. Neurosci.* 38, 93–107 (2018).
34. Chen, J. *et al.* High-Frequency repetitive transcranial magnetic stimulation enhances white matter integrity in a rat model of ischemic stroke: A diffusion tensor imaging study using tract-based spatial statistics. *NeuroImage* 311, 121204 (2025).
35. Wang, J. *et al.* Enhanced autophagy interacting proteins negatively correlated with the activation of apoptosis-related caspase family proteins after focal ischemic stroke of young rats. *BMC Neurosci* 23, 55 (2022).
36. Chen, J. *et al.* Intravenous Administration of Human Umbilical Cord Blood Reduces Behavioral Deficits After Stroke in Rats. *Stroke* 32, 2682–2688 (2001).
37. Wang, Y. *et al.* Prim-O-glucosylcimifugin ameliorates aging-impaired endogenous tendon regeneration by rejuvenating senescent tendon stem/progenitor cells. *Bone Res* 11, 54 (2023).
38. He, S. *et al.* Neuroprotective effects of chlorogenic acid: Modulation of Akt/Erk1/2 signaling to prevent neuronal apoptosis in Parkinson's disease. *Free Radical Biology and Medicine* 222, 275–287 (2024).
39. Yeh, S.-J. *et al.* Neuroanatomy- and Pathology-Based Functional Examinations of Experimental Stroke in Rats: Development and Validation of a New Behavioral Scoring System. *Front. Behav. Neurosci.* 12, 316 (2018).

Figures

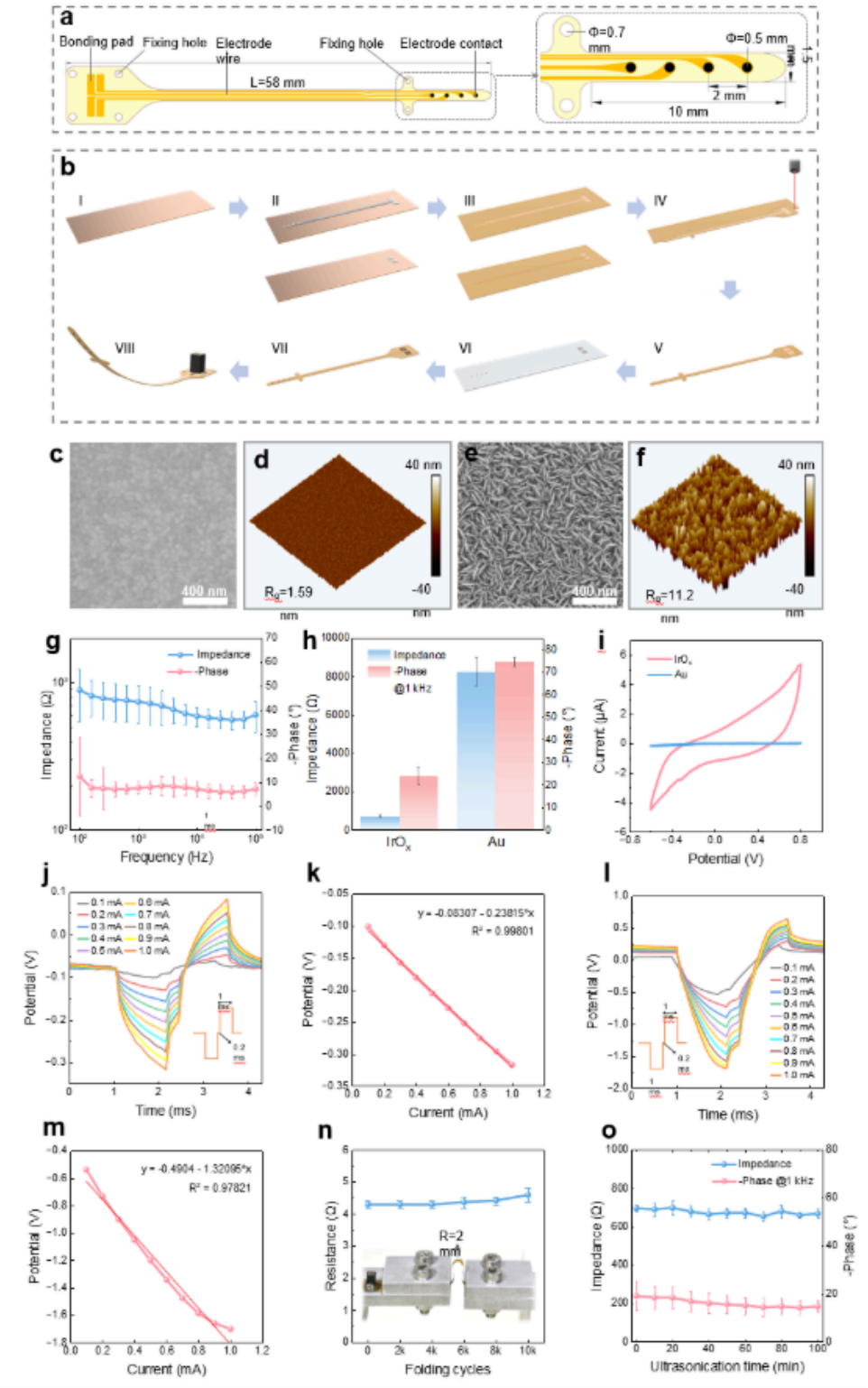


Figure 1

Design, fabrication, and in vitro characterization of the flexible nanoporous IrOx epidural interface.

a) Layout and dimensions of the flexible four-contact cervical epidural interface. b) Schematic illustration of the device-fabrication process. c,d) Representative scanning electron microscopy (SEM) and atomic force microscopy (AFM) images of the gold (Au) electrode surface. e,f) Representative SEM

and AFM images of the nanoporous IrOx-coated electrode surface. g) Electrochemical impedance magnitude and phase spectra of the Au and IrOx-modified electrodes. h) Impedance magnitude and phase at 1 kHz. i) Cyclic voltammetry curves of the Au and IrOx-modified electrodes. j,l) Representative voltage transients of the IrOx-modified (j) and Au (l) electrodes under symmetric biphasic current pulses of increasing amplitude. k,m) Relationships between applied current and maximum cathodic polarization used to estimate the maximum current (Imax) and charge-injection capacity of the IrOx-modified (k) and Au (m) electrodes. n) Resistance of the IrOx-modified flexible devices during 10,000 bending cycles at a bending radius of 2 mm. o) Relative changes in impedance magnitude and phase during 100 min of ultrasonication. Quantitative data are presented as mean ± SD from 12 independently fabricated devices (n = 12).

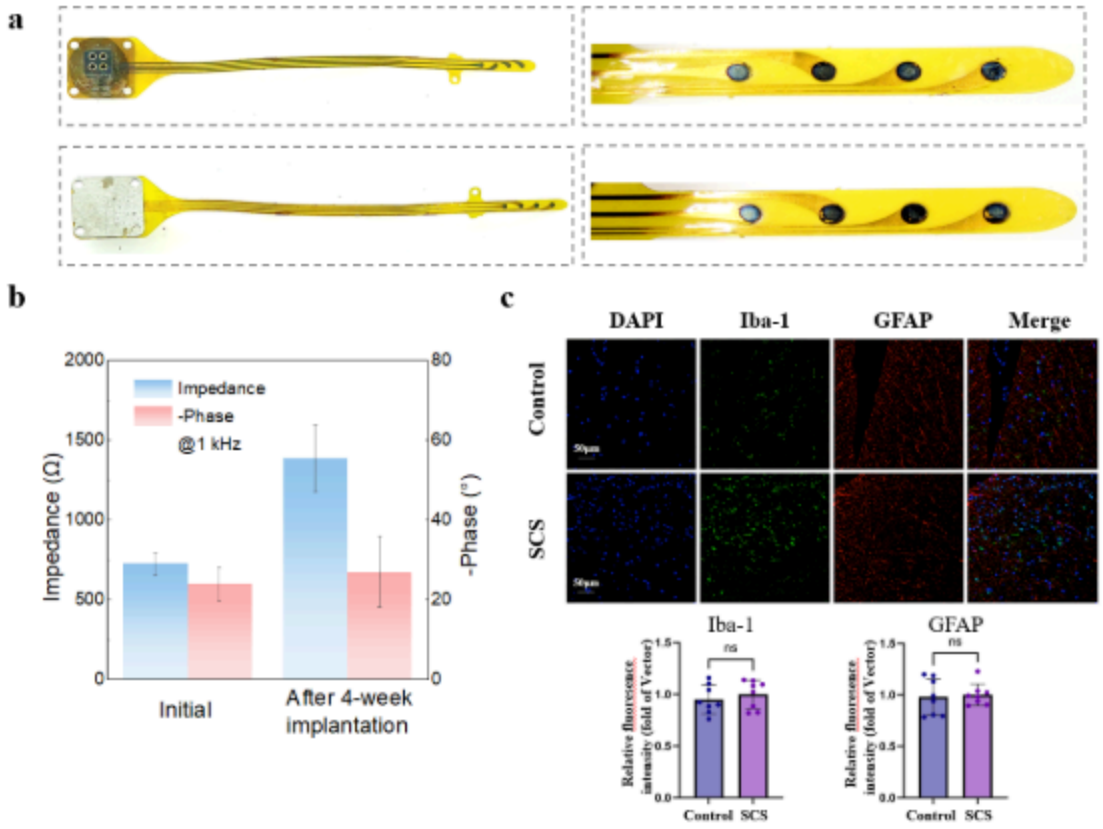


Figure 2

Four-week in vivo functional retention and local cervical tissue response of the flexible IrOx interface.

a) Representative photographs of devices retrieved after four weeks in vivo, showing preservation of the overall device geometry, conductive traces, and electrode-contact sites. b) Electrode impedance magnitude and phase at 1 kHz before implantation and after four weeks in vivo (n = 6 devices). Measurements before and after implantation were obtained from the same devices. c) Representative immunofluorescence images of DAPI, Iba1, GFAP, and merged channels in cervical spinal cord sections from the electrode-implanted SCS group and non-implanted MCAO/R controls, together with the

corresponding quantification of Iba1 and GFAP fluorescence intensities. Data are presented as mean ± SEM. ns, not significant. Scale bars, 50 μm.

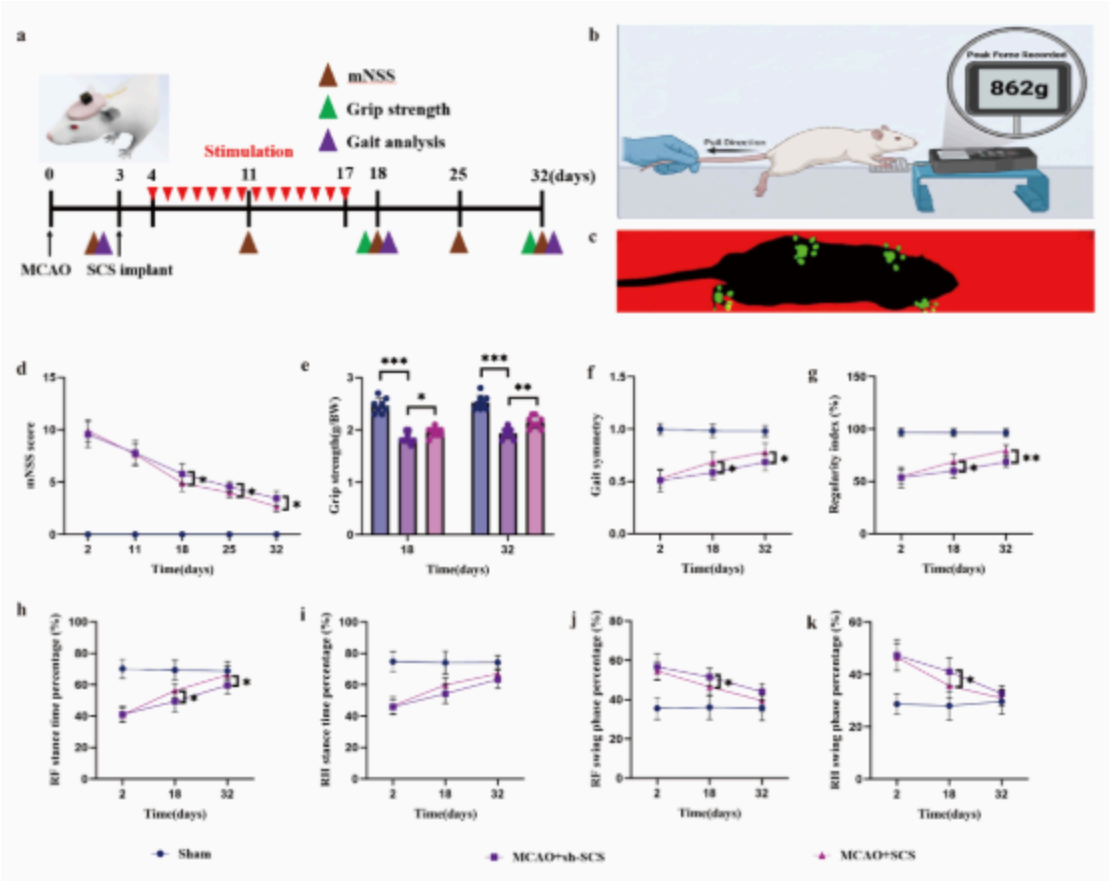


Figure 3

Cervical SCS improves neurological and motor outcomes after MCAO/R. a) Experimental timeline showing MCAO on day 0, electrode implantation on day 3, and daily SCS from days 4 to 17. b,c) Schematics of forelimb grip-strength testing (b) and automated gait analysis (c). d) Modified Neurological Severity Score (mNSS) on days 2, 11, 18, 25, and 32. e) Forelimb grip strength normalized to body weight on days 18 and 32. f–k) Gait symmetry index (f), regularity index (g), right forelimb and hindlimb stance-phase durations (h,i), and right forelimb and hindlimb swing-phase durations (j,k) on days 2, 18, and 32. Data are presented as mean ± SEM; n = 8 animals per group. Longitudinal outcomes were analyzed using two-way repeated-measures ANOVA followed by Tukey's multiple-comparisons test. Unless otherwise indicated by brackets, asterisks denote comparisons between the MCAO+SCS and MCAO+sh-SCS groups at the corresponding time point. *P < 0.05, **P < 0.01, and ***P < 0.001.

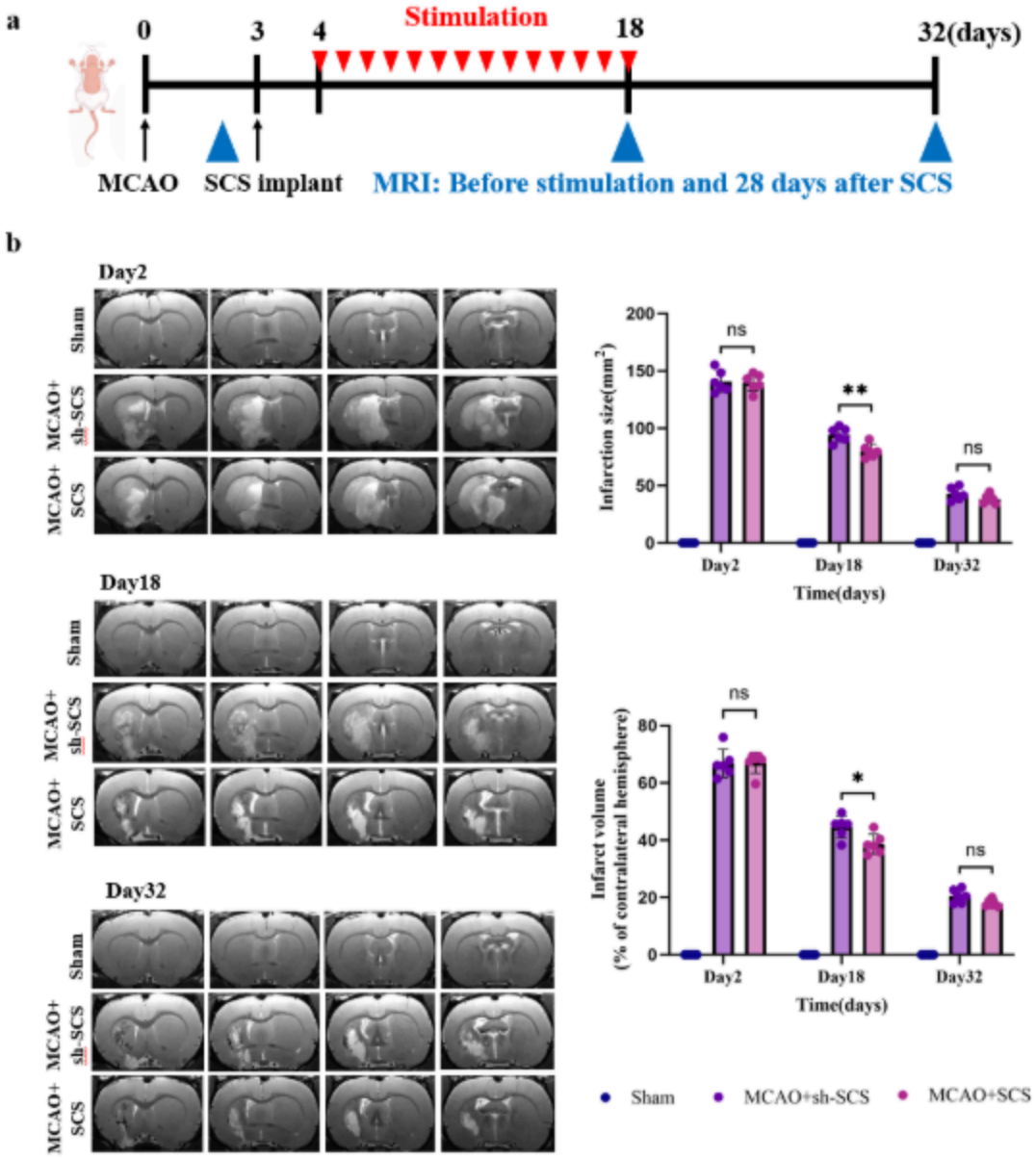


Figure 4

Longitudinal T2-weighted MRI of ischemic lesion burden after cervical SCS. a) Experimental timeline showing MCAO on day 0, T2-weighted MRI on days 2, 18, and 32, electrode implantation on day 3, and daily SCS from days 4 to 17. b) Representative coronal T2-weighted images from the Sham, MCAO+sh-SCS, and MCAO+SCS groups on days 2, 18, and 32, with quantification of absolute T2-defined lesion volume and lesion volume normalized to the contralateral hemisphere. Data are presented as mean ± SEM; n = 6 animals per group. Longitudinal outcomes were analyzed using two-way repeated-measures ANOVA followed by Tukey's multiple-comparisons test. Asterisks denote comparisons between the MCAO+SCS and MCAO+sh-SCS groups at the corresponding time point. ns, not significant; *P < 0.05 and **P< 0.01.

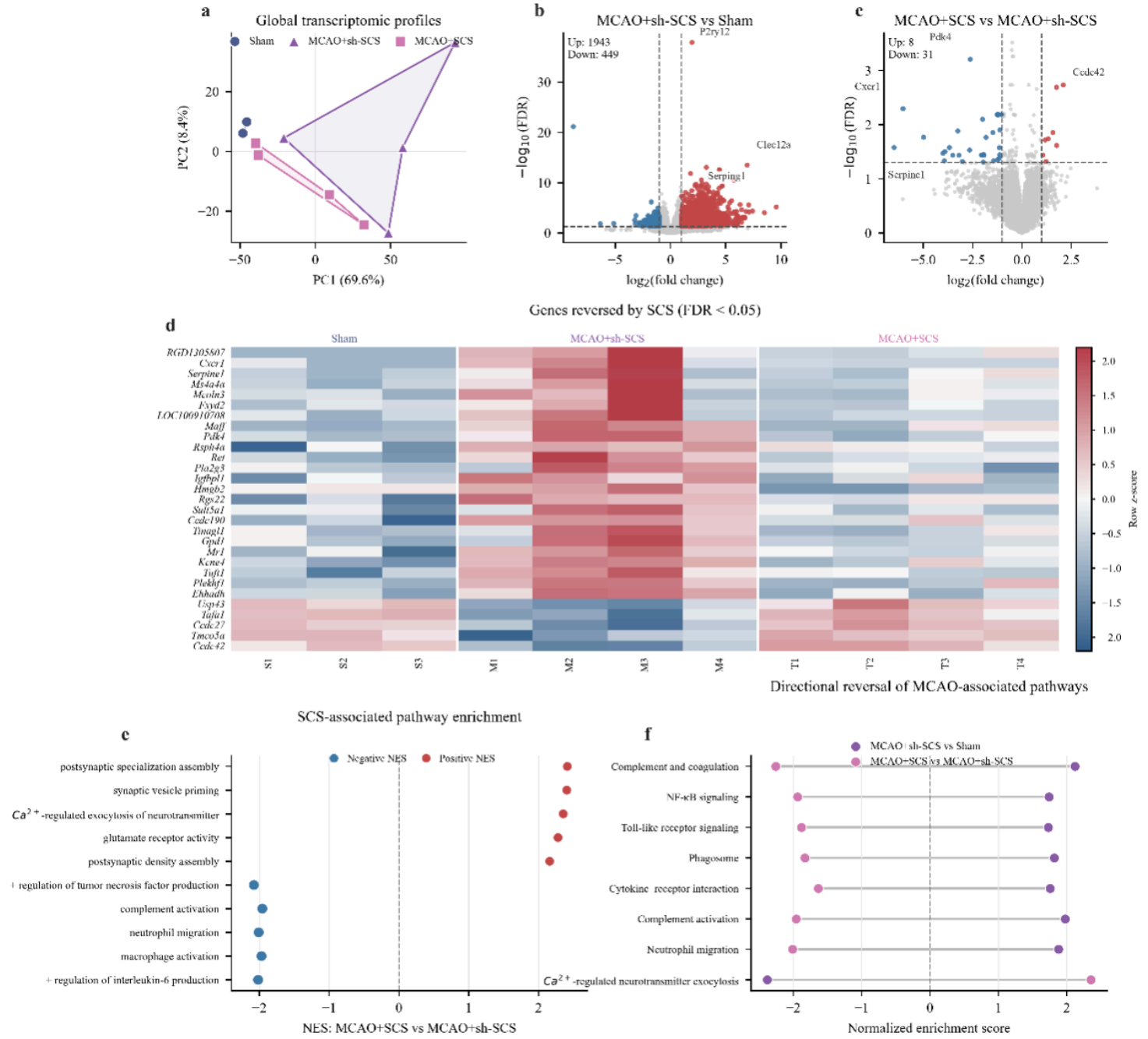


Figure 5

Cervical spinal cord stimulation reprograms post-stroke cortical transcriptional responses. **a**, Principal component analysis of cortical RNA-sequencing profiles from Sham (n = 3), MCAO+sh-SCS (n = 4), and MCAO+SCS (n = 4) animals. Points represent individual animals. **b,c**, Volcano plots for MCAO+sh-SCS versus Sham (b) and MCAO+SCS versus MCAO+sh-SCS (c). DEGs were defined as FDR < 0.05 and |log2 fold change| > 1; red, blue, and grey denote upregulated, downregulated, and non-significant genes, respectively. **d**, Row-scaled heatmap of 29 DEGs showing opposite changes across the two comparisons. S, Sham; M, MCAO+sh-SCS; T, MCAO+SCS. **e**, Gene Ontology gene set enrichment analysis of MCAO+SCS versus MCAO+sh-SCS. Dot position, size, and color indicate NES, −log10(FDR), and

enrichment direction, respectively. **f**, NES values of representative MCAO-associated pathways across the two comparisons, showing reversal after SCS. All displayed pathways in e,f had FDR < 0.05.

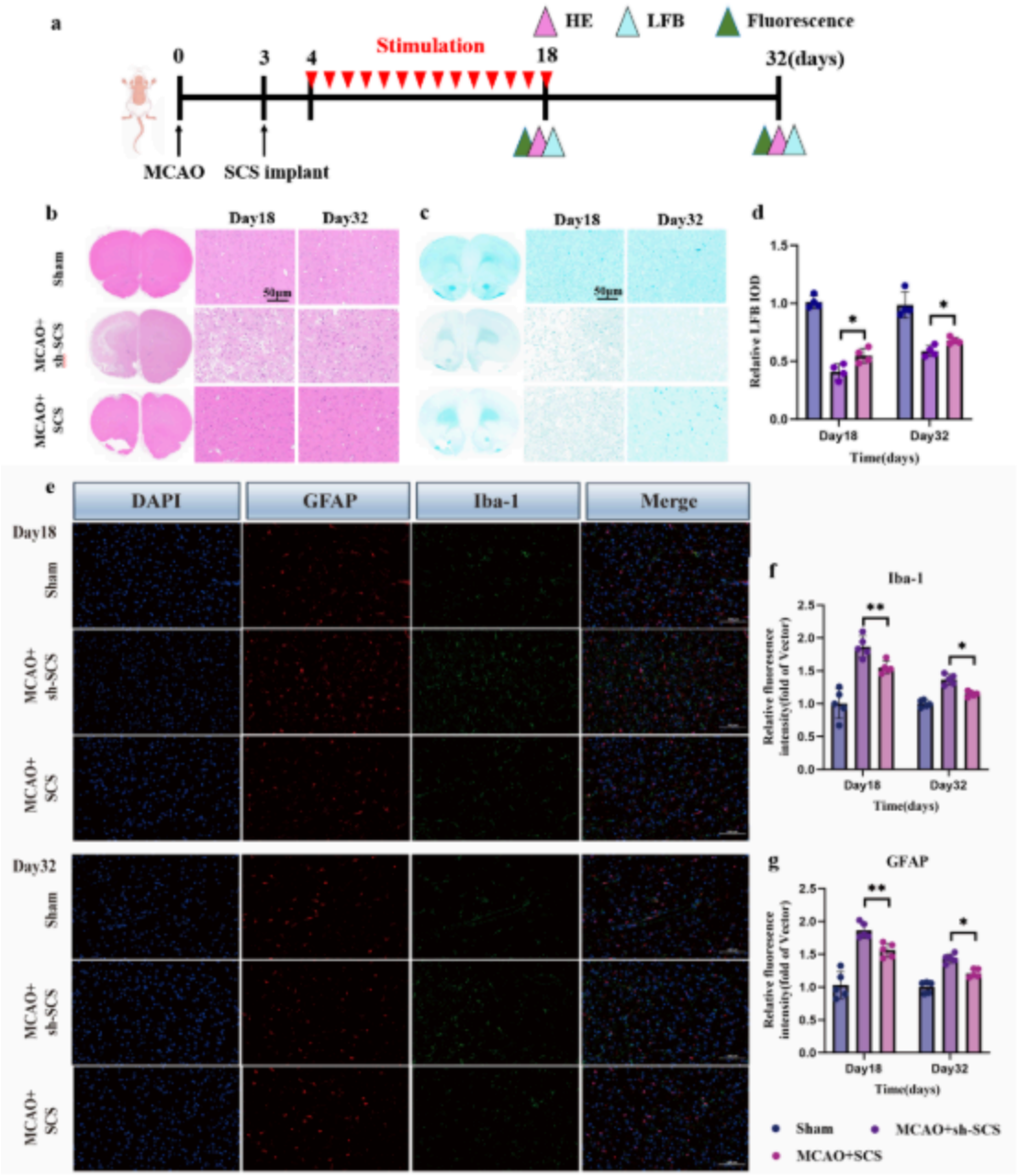


Figure 6

Histopathological, myelin and glial changes following cervical spinal cord stimulation after MCAO/R. **a**, Experimental timeline showing MCAO induction, electrode implantation, cervical spinal cord stimulation, and tissue collection on days 18 and 32. **b**, Representative H&E-stained coronal brain sections and higher-magnification images of the ipsilateral motor cortex. **c**, Representative LFB-stained sections showing myelin integrity in the ipsilateral motor cortex. **d**, Quantification of relative LFB integrated optical density (IOD). **e**, Representative immunofluorescence images of DAPI (blue), GFAP (red), Iba-1 (green), and merged channels in the ipsilateral motor cortex on days 18 and 32. **f, g**, Quantification of the relative fluorescence intensities of Iba-1 (f) and GFAP (g). Data are presented as mean ± SEM; n = 4 animals per

group for H&E and LFB quantification and n = 5 animals per group for immunofluorescence quantification. Statistical comparisons were performed using two-way ANOVA followed by Tukey's multiple-comparisons test. *P < 0.05 and **P< 0.01. MCAO+sh-SCS indicates MCAO with sham stimulation; MCAO+SCS indicates MCAO with active cervical spinal cord stimulation. Scale bars, 50 μm in b, c and 100 μm in e.

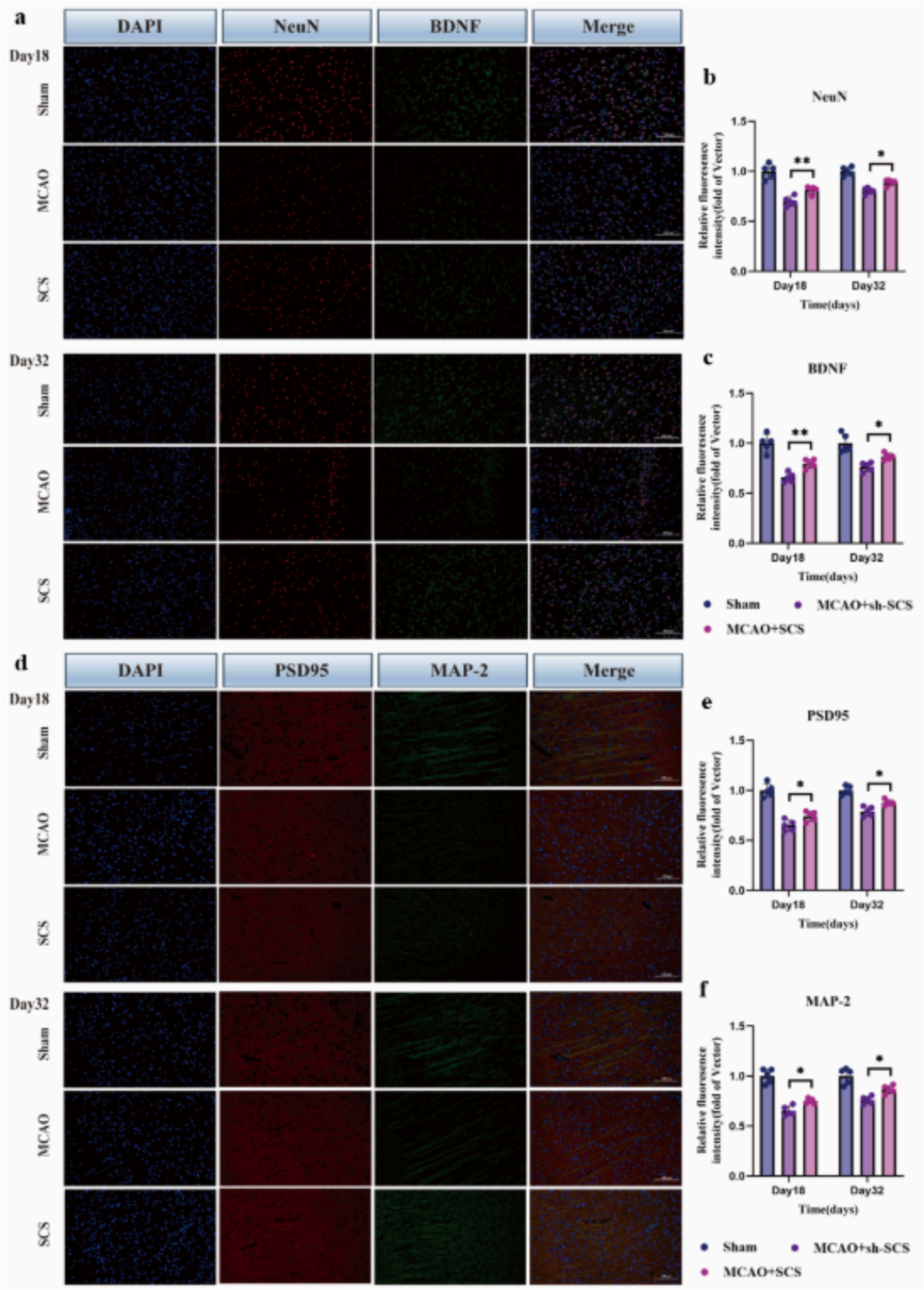


Figure 7

Cervical spinal cord stimulation preserves neuronal integrity and increases neurotrophic and synaptic protein expression after MCAO/R.
a, Representative immunofluorescence images of DAPI (blue), NeuN (red), BDNF (green), and merged staining in the ipsilateral M1 cortex of the Sham, MCAO+sh-SCS, and MCAO+SCS groups on Day 18 and Day 32. **b, c**, Quantification of the relative fluorescence intensities of NeuN (b) and BDNF (c). **d**, Representative immunofluorescence images of DAPI (blue), PSD95 (red), MAP-2 (green), and merged staining in the ipsilateral M1 cortex on Day 18 and Day 32. **e, f,** Quantification of the relative fluorescence intensities of PSD95 (e) and MAP-2 (f). Data are presented as mean ± SEM; *n*= 5 animals per group at each time point. Statistical significance was assessed using two-way ANOVA followed by Tukey's multiple-comparisons test. The brackets indicate comparisons between the MCAO+sh-SCS and MCAO+SCS groups. **P*< 0.05 and ***P* < 0.01. Scale bars are shown in the images.

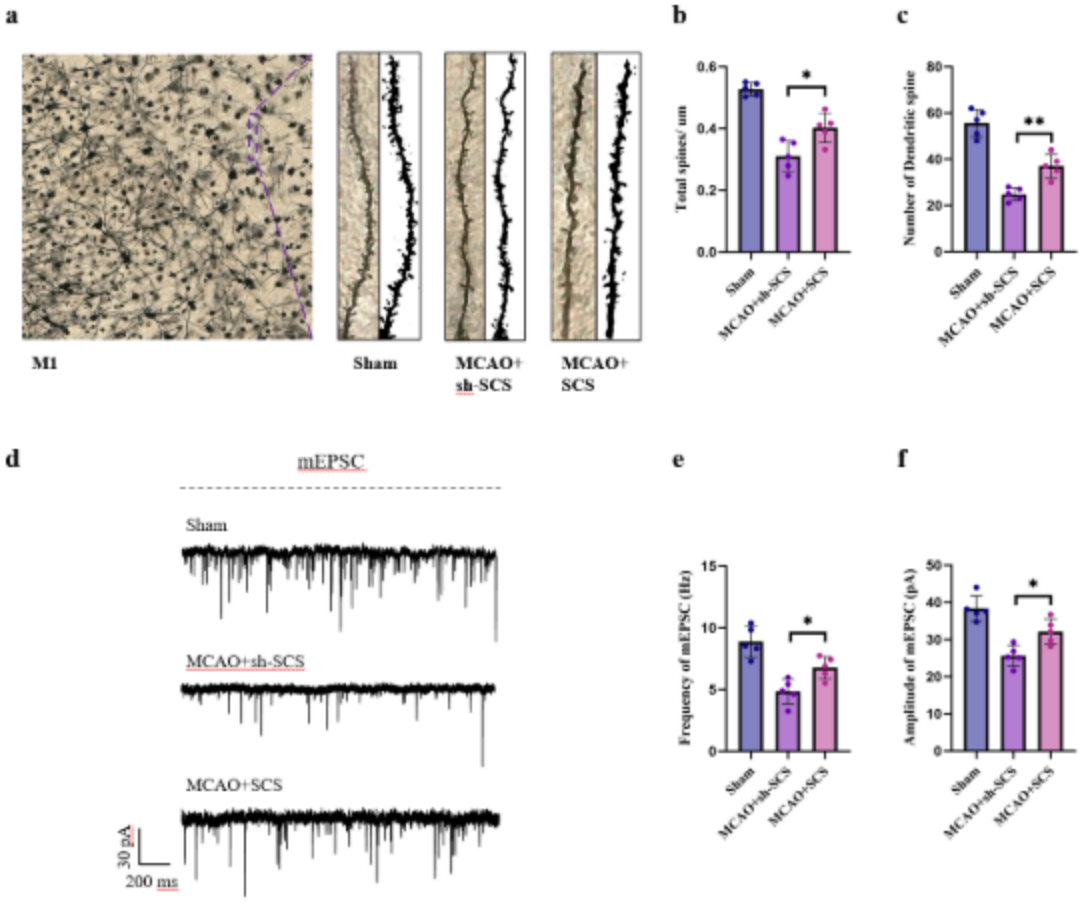


Figure 8

Cervical spinal cord stimulation partially restores dendritic spine density and excitatory synaptic transmission after MCAO/R. **a**, Representative Golgi–Cox staining image of pyramidal neurons in the ipsilateral M1 cortex and enlarged images of secondary dendritic segments from the Sham, MCAO+sh-SCS, and MCAO+SCS groups after 14 days of stimulation. Corresponding binary reconstructions are shown beside each dendritic segment. **b, c**, Quantification of dendritic spine density, expressed as the number of spines per micrometre (b), and total dendritic spine number (c). **d**, Representative miniature

excitatory postsynaptic current (mEPSC) traces recorded from layer V pyramidal neurons in the ipsilateral M1 cortex. Scale bars, 30 pA and 200 ms. **e, f**, Quantification of mEPSC frequency (e) and amplitude (f). Data are presented as mean ± SEM; *n* = 5 animals per group. Statistical significance was assessed using one-way ANOVA followed by Tukey's multiple-comparisons test. Brackets denote comparisons between the MCAO+sh-SCS and MCAO+SCS groups. **P* < 0.05 and ***P*< 0.01.